Icarus **141**, 179–193 (1999)
Article ID icar.1999.6175, available online at http://www.idealibrary.com on IDEAL®

Near-Surface Temperatures on Mercury and the Moon and the Stability of Polar Ice Deposits[1]

Ashwin R. Vasavada[2]

Division of Geological and Planetary Sciences, California Institute of Technology, Pasadena, California 91125
E-mail: ash@mvacs.ess.ucla.edu.

David A. Paige

Department of Earth and Space Sciences, University of California, Los Angeles, Los Angeles, California 90095-1567

and

Stephen E. Wood

Department of Atmospheric Sciences, University of Washington, Seattle, Washington 98195-1640

Received July 16, 1998; revised February 19, 1999

In order to assess the thermal stability of polar ice deposits, we present model calculated temperatures of flat surfaces and surfaces within bowl-shaped and flat-floored polar impact craters on Mercury and the Moon. Our model includes appropriate insolation cycles, realistic crater shapes, multiple scattering of sunlight and infrared radiation, and depth- and temperature-dependent regolith thermophysical properties. Unshaded water ice deposits on the surface of either body are rapidly lost to thermal sublimation. A subsurface water ice deposit is stable within 2° latitude of the Moon's poles. Meter-thick water ice deposits require billions of years to sublime if located in the permanently shaded portions of flat-floored craters within 10° latitude of the poles of Mercury and 13° latitude of the poles of the Moon. Results for craters associated with radar features on Mercury are consistent with the presence of stable water ice deposits if a thin regolith layer thermally insulates deposits at lower latitudes and within smaller craters. A regolith cover would also reduce losses from diffusion, ion sputtering, impact vaporization, and H Lyα and is implied independently by the radar observations. Permanently shaded areas near the Moon's poles are generally colder than those near Mercury's poles, but the Moon's obliquity history, its orbit through Earth's magnetospheric tail, and its radar-opaque regolith may limit the volume and radar detectability of ice deposits there. © 1999 Academic Press

Key Words: **Mercury; moon; ices.**

I. INTRODUCTION AND BACKGROUND

A relatively old idea in planetary science, that volatiles may be cold trapped in permanently shaded regions near the poles of the Moon and Mercury (Watson *et al.* 1961, Thomas 1974), was revitalized when strong, highly depolarized (circular polarization ratio > 1) radar echoes were received from the poles of Mercury (Slade *et al.* 1992, Harmon and Slade 1992, Butler *et al.* 1993). The anomalous radar response was interpreted to indicate ice deposits by analogy with radar returns from the icy galilean satellites and Mars' south polar residual ice cap (Goldstein and Morris 1975, Muhleman *et al.* 1991). Water is the favored composition because of its relatively high cosmic abundance and low vapor pressure. The inverted polarization ratio is thought to arise from volume scattering by density variations, voids, or particles within weakly absorbing water ice. The radar beam is deflected 180° incrementally by a series of forward scattering events, each of which preserves the sense of polarization (Hagfors *et al.* 1997). The radar cross section may be further enhanced by the coherent backscatter opposition effect (Hapke 1990). Recent observations have shown that terrestrial ice fields produce a similar radar response (Rignot 1995, Haldemann 1997). The exact scattering mechanisms operative in each environment and the physical structures that produce them are still debated (e.g., Hagfors *et al.* 1997). Considerations of the possibility of volatiles other than cubic water ice can be found in Sprague *et al.* (1995), Butler (1997), and Jenniskens and Blake (1996).

Two experiments have searched for a similar radar response from the Moon's poles. The Clementine–Deep Space Network bistatic radar experiment claimed to detect a slightly enhanced,

[1] Contribution 5768 from the Division of Geological and Planetary Sciences, California Institute of Technology, Pasadena, CA 91125.

[2] Present address: Department of Earth and Space Sciences, University of California, Los Angeles, Los Angeles, CA 90095-1567.

0019-1035/99 $30.00
Copyright © 1999 by Academic Press
All rights of reproduction in any form reserved.

slightly depolarized signal from a region near the south pole (Nozette *et al.* 1996). Higher resolution Arecibo radar observations by Stacy *et al.* (1997) revealed no extensive areas with anomalous radar properties near either pole. They did detect ice-like radar properties for several small (∼1 km) regions, but some of these were in sunlit areas and may be explained better by surface roughness effects. The lunar experiments had a less favorable geometry than the observations of Mercury but were capable of probing permanently shaded areas. The sub-Earth latitude was 4–6° during the lunar experiments, half that of the Mercury experiments. Including the finite size of the solar disk and each body's solar obliquity, the edge of the solar disk rises 1.85° above the horizon at the Moon's poles and 1.6° above Mercury's. Earth-based radar experiments see further into permanently shaded areas on Mercury, but cannot completely probe the polar terrain of either body. For example, an observer must be ∼22° above the horizon to see the bottom of a 10-km crater. While lunar radar results are presently inconclusive, the neutron spectrometer aboard the Lunar Prospector spacecraft has found evidence for polar water ice deposits (Feldman *et al.* 1998). The possibility that polar ices are present on both bodies is intriguing considering their different histories and environments.

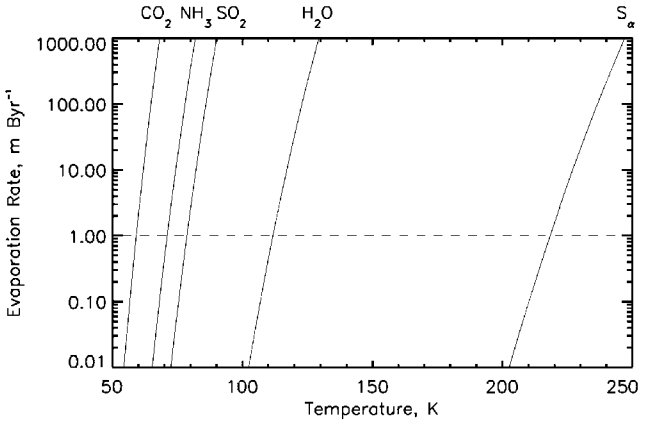

FIG. 1. Evaporation rates into a vacuum as functions of temperature for CO_2, NH_3, SO_2, cubic H_2O, and S_α (solid orthorhombic sulfur) ices. Vapor pressure data were taken from the *CRC Handbook of Chemistry and Physics* (Lide 1993), Bryson *et al.* (1974), and Moses and Nash (1991). The calculation of evaporation rates follows Watson *et al.* (1961). The dashed line marks the rate at which one meter of ice would survive for 1 billion years. The curves cross this line at 59, 71, 78, 112, and 218 K.

Several recent studies have sought a deeper understanding of the sources, evolution, and sinks of volatiles on Mercury and the Moon (Morgan and Shemansky 1991, Potter 1995, Rawlins *et al.* 1995, Butler 1997, Killen *et al.* 1997). Volatiles are delivered to their surfaces by impactors and planetary outgassing. Volatiles also are derived from the regolith by impact vaporization, photon-stimulated desorption, and ion sputtering of surface minerals with subsequent chemical reactions. Calculations show that water retained from meteoroid or comet impacts or water produced through solar wind sputtering alone probably could produce detectable deposits on either body. Molecules in sunlit areas will hop in ballistic, collisionless trajectories until lost by photodissociation, photoionization, other less important exospheric loss processes, or landing in a permanently shaded area. Butler (1997) found comparable time scales for loss by photodestruction and loss by cold trapping for both water and CO_2. Therefore, a fraction of molecules delivered to either body's surface will survive other loss processes and form polar deposits. Watson *et al.* (1961) noted that once deposits form, their loss rate cannot exceed the rate of thermal sublimation (evaporation) from the condensed phase. Figure 1 shows the sublimation rates of several volatiles as functions of temperature. These rates are used to gauge the stability of volatiles in this study, although actual loss rates may be lower for several reasons. A fraction of the sublimed molecules may recondense before being lost to photodestruction (Killen *et al.* 1997). If an ice layer is covered by a thin regolith layer, the ice would be protected from peak surface temperatures and surface loss processes. Then the loss rate could be limited by diffusion through the regolith cover (Salvail and Fanale 1994, Killen *et al.* 1997).

Because of the importance of thermal sublimation, the temperatures of polar surfaces that may act as volatile cold traps are the key factor that determines where ice deposits will condense, how long deposits will survive, and what their composition may be. Thermal modeling by Paige *et al.* (1992) showed that the temperatures of flat surfaces near Mercury's poles preclude the stability of exposed water ice deposits (i.e., polar caps) due to high sublimation rates. However, the temperatures within permanently shaded, shallow topographic depressions near the poles permit the stability of meter-thick, cubic water ice deposits over the age of the Solar System (Paige *et al.* 1992, Ingersoll *et al.* 1992). Thermal models of the Moon's poles predict that sites capable of sustaining ice deposits should exist there also (Ingersoll *et al.* 1992, Salvail and Fanale 1994).

Arecibo radar maps of Mercury's poles (Harmon *et al.* 1994) place many radar features within polar impact craters observed by Mariner 10. The ice-like radar response of the locations and their correlation with areas of permanent shadow (and thus low temperature) make a compelling case for the presence of ice deposits on Mercury. While previous thermal modeling studies have verified the thermal stability of water ice deposits at these locations, the simplifications included in the models limit their usefulness when making quantitative comparisons with the radar observations. In this paper we present a more complete and systematic study of the temperatures near the poles of Mercury and the Moon. We present new model calculations of the surface and subsurface temperatures within bowl-shaped and flat-floored polar impact craters using improved estimates of surface thermophysical properties and impact crater shapes. We also specifically model craters on Mercury observed to produce anomalous radar responses and lunar craters recently identified in Clementine imagery and ground based radar maps. We begin by describing our thermal model for flat surfaces and exploring the effects of thermophysical properties on subsurface temperatures. We then describe our scattering model for impact craters. Finally we present our results, compare them with the high

resolution Arecibo radar maps of Mercury, and discuss several implications for ice deposits on Mercury and the Moon.

II. THERMAL MODELING

A. Temperatures of Flat Surfaces: 1-D Thermal Model

The temperature response of surface and subsurface layers to solar, infrared, and internal energy fluxes is determined by their bulk thermophysical properties, namely their solar albedo, infrared emissivity, density, thermal conductivity, and heat capacity. The properties of the regoliths of Mercury and the Moon have been derived from ground- and spacecraft-based observations, lunar *in situ* measurements, and returned samples. The major results are that (i) the near surface layers on Mercury and the Moon are similar and spatially uniform over large scales, (ii) the mean temperature increases with depth in the top few centimeters, (iii) the density increases with depth as determined by radio emissions over a range of wavelengths, and (iv) the thermophysical properties change abruptly near the surface, as evidenced by rapid cooling of the uppermost layer just after sunset (or eclipse) followed by slow cooling of the surface during the night. Accordingly, thermal models that best match observations have modeled the regoliths as loosely packed particulate material with temperature- and depth-dependent thermophysical properties (Linsky 1966, Morrison 1970, Keihm and Langseth 1973, Cuzzi 1974, Ledlow *et al.* 1992, Mitchell and de Pater 1994 and references therein).

Mitchell and de Pater (1994) constructed a two-layer model that is largely consistent with the variety of lunar measurements and the radiometry of Mercury's surface from Mariner 10. Their model consists of a 2-cm-thick top layer that is highly insulating and a lower layer that is more dense and conductive. Thermal radiation between grains, which is strongly temperature dependent, dominates solid conduction (within and between grains) at temperatures above ~350 K in the top layer. Solid (phonon) conductivity is dominant within the lower layer. The sizes and packing of grains, rather than composition, more likely accounts for the different modes of conduction within each layer. The widespread presence of this two-layer stratigraphy can be explained by ubiquitous micrometeorite bombardment that churns the top layer and compresses the lower layer.

Our model, like the model of Mitchell and de Pater (1994), consists of two layers that differ in thermal conductivity and bulk density. The top layer extends from the surface to a depth of 2 cm and has a bulk density of 1300 kg m^{-3}. The lower layer has a bulk density of 1800 kg m^{-3}. The thermal conductivity has the form $k(T) = k_c[1 + \chi(T/350)^3]$, where T is temperature, k_c is the solid conductivity, and χ is the ratio of radiative to solid conductivity at a temperature of 350 K. We chose values of k_c and χ that best represent the range of measured and derived values. Our top layer has the values of a lunar regolith sample from Apollo 12, with $k_c = 9.22 \times 10^{-4}$ W m^{-1} K^{-1} and $\chi = 1.48$ (Cremers and Birkebak 1971). Following Mitchell and de Pater (1994), the bottom layer has $k_c = 9.3 \times 10^{-3}$ W m^{-1} K^{-1} and $\chi = 0.073$. The lower value of χ is primarily due to the larger solid conductivity. The temperature dependence of the heat capacity is taken from Ledlow *et al.* (1992). They derived an expression based on lunar sample measurements but applicable to the range of temperatures on Mercury. We assume an albedo of 0.10 and an infrared emissivity of 0.95. The internal heat fluxes of Mercury and the Moon are assumed to be 0.020 W m^{-2} (Schubert *et al.* 1988) and 0.033 W m^{-2} (Langseth *et al.* 1972, 1976), respectively. The albedo, emissivity, and internal heat fluxes are both uncertain and spatially variable. However, reasonable variations in them do not significantly change our calculated temperatures.

We use a time stepping, finite difference model to solve the thermal diffusion equation in one dimension. Depending on the assumed thermophysical properties, between 12 and 30 model layers are used to resolve the shape and depth of the thermal wave in the subsurface. The orbital position and orientation of the body is updated at each time step. The size of the solar disk and darkening of the solar limb follow the formulations of Allen (1973). The temperature of the surface (extrapolated from the top three layers to the actual surface using a second order scheme) is determined by an instantaneous balance of the incident solar, conducted, emitted infrared, and internal energy fluxes. The temperature gradient at the deepest model layers is forced to equal that produced by the internal heat flux. The model time step and number of model layers are chosen to resolve the 2-cm physical layer and to extend well below the depth of diurnal temperature variations. The model is run until the bottom layers equilibrate.

Because of Mercury's 3:2 spin orbit resonance, one diurnal period at any point on Mercury's surface is equal to 3 sidereal days, or 2 sidereal years, or 176 Earth days. Consequently, longitudes 0° and 180° always experience noon at perihelion, while longitudes 90° and 270° always experience noon at aphelion. The temperature variation within the Moon's surface layers has a diurnal and seasonal component. Our lunar model temperatures are output over a span of 12 diurnal periods, or nearly 1 lunar year. Each diurnal period is 29.5 Earth days. Because the Moon's solar obliquity is only 1.54°, temperatures at low latitudes are determined predominantly by the diurnal period and vary little with season. Temperatures of surfaces very close to the poles have a large seasonal variation.

B. Temperatures of Flat Surfaces: Model Results

We ran our two-layer model with the thermophysical properties described above (hereafter called Model TWO). We also ran one-layer models which use only the properties of the bottom (Model BOT) or top (Model TOP) layer of the two-layer model. These results show the effects of temperature- and depth-dependent thermophysical properties. They also constrain the latitude range of surface or subsurface ice deposits unaffected by reflections, emissions, or shadowing from surrounding topography (i.e., polar caps). All calculations presented in this section neglect the internal heat flux because its contribution

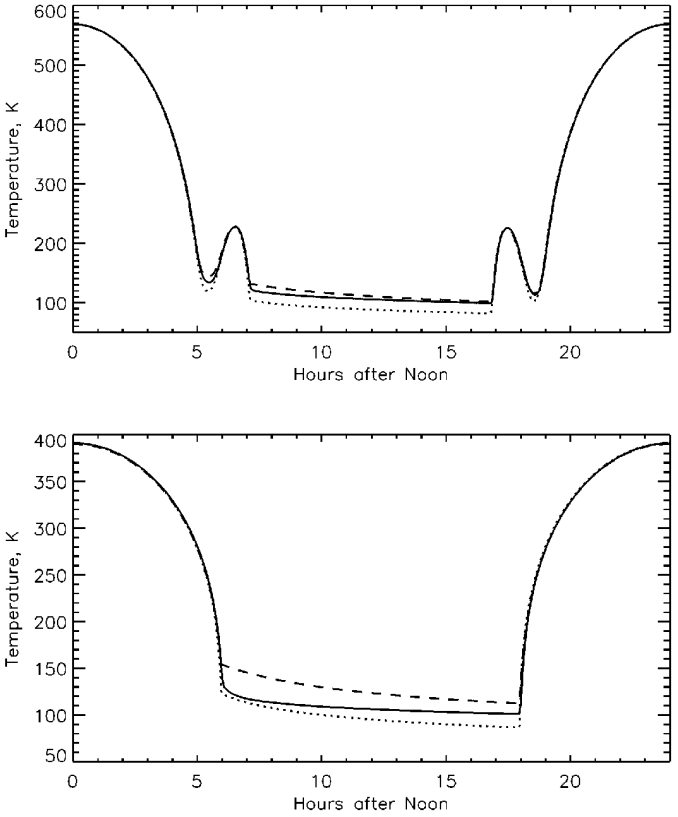

FIG. 2. Surface temperature as a function of local time at the equators of Mercury (top) and the Moon (bottom). Results of the two-layer model (Model TWO) are plotted as solid lines. The entire surface layer in Model BOT (dashed) has the thermophysical properties of the high thermal inertia, bottom layer of the two-layer model. The entire surface layer in Model TOP (dotted) has the thermophysical properties of the low thermal inertia, top layer of the two-layer model. The Mercury results are for 90°W longitude. During perihelion Mercury's orbital angular velocity briefly exceeds its spin rate, resulting in a brief secondary sunrise and sunset at this longitude.

is negligible at temperatures above ~30 K. Therefore temperature is constant with depth below the penetration depth of the sunlight-driven temperature oscillation.

Figure 2 shows surface temperature as a function of local time at the equators of Mercury and the Moon. Temperatures are in radiative equilibrium during the day, but at night temperatures are determined by the bulk thermal inertia, $(k\rho c)^{1/2}$, of the surface layers. Although the bulk thermal inertia of Model TWO is dominated by that of the lower layer, its surface temperature drops quickly after sunset as the top layer loses its heat. It subsequently cools slowly during the night as stored heat is conducted inefficiently through the top layer and is radiated at relatively lower temperatures.

Figure 3 shows the diurnal temperature variation below Mercury's surface at (0°N, 0°W) and (85°N, 0°W). When the radiative (temperature dependent) component of the thermal conductivity is unimportant (Model BOT), heat is conducted with equal efficiency into the subsurface during the day and out at night and the mean temperature is nearly constant with depth. When conductivity is a strong function of temperature (Model TOP), energy conducted downward along a temperature gradient during the day is released along a steeper gradient of opposite sign at night. In this case the mean temperature increases with depth and the equilibrium temperature at depth is accordingly higher. Below the 2-cm top layer, the temperature profiles of Model TWO resemble those of Model BOT shifted to higher temperatures by the presence of the top layer. At (0°N, 0°W) the temperatures at depth in Models BOT, TOP, and TWO are 365, 463, and 427 K, respectively. The top layer in model TWO significantly affects temperatures at depth even though it is thin compared to the penetration depth of the temperature oscillation.

Figure 4 shows the temperature variation below the Moon's surface at 0°N and 85°N. The effects of temperature-dependent conductivity are less prominent because of lower temperatures on the Moon. Also, because of the shorter diurnal period, temperature oscillations penetrate less deeply and are more influenced by the 2-cm top layer. In fact, temperatures at depth in

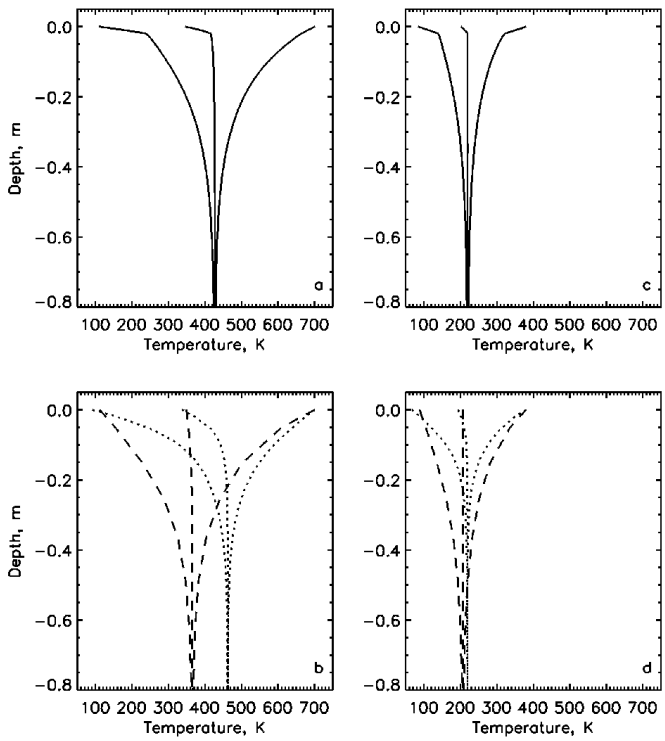

FIG. 3. Diurnal minimum, mean, and maximum temperatures as functions of depth on Mercury. These curves represent the extreme and mean temperatures experienced at each depth (they are not instantaneous profiles). (a) Results of our two-layer model (Model TWO) at (0°N, 0°W). The top, 2-cm layer has a small but strongly temperature-dependent thermal conductivity. The lower layer has a greater conductivity with little temperature dependence. (b) Results from models in which the entire surface layer has the thermophysical properties of the bottom (Model BOT, dashed) or top (Model TOP, dotted) layer of the two-layer model. (c) Model TWO at (85°N, 0°W). (d) Models BOT and TOP at (85° N, 0° W).

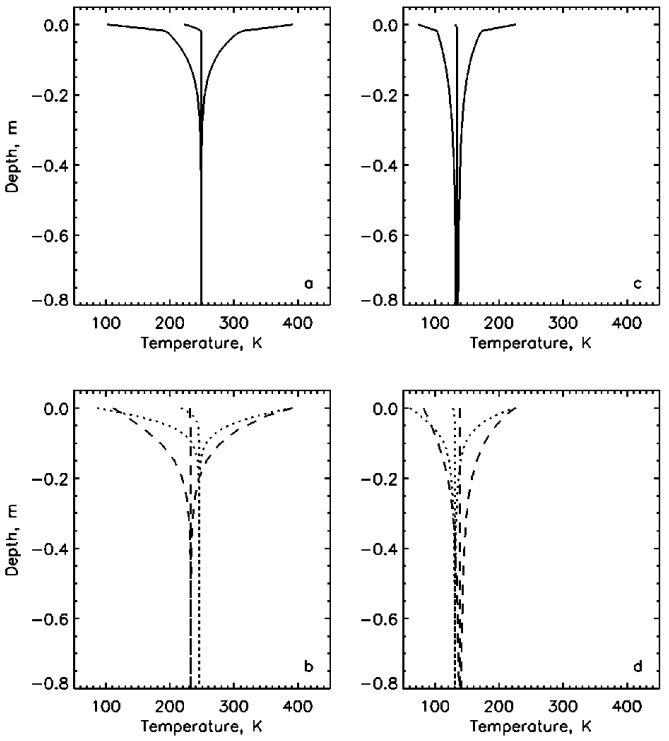

FIG. 4. Diurnal minimum, mean, and maximum temperatures as functions of depth on the Moon. These curves represent the extreme and mean temperatures experienced at each depth (they are not instantaneous profiles). (a) Results of our two-layer model (Model TWO) at 0°N. The top, 2-cm layer has a small but strongly temperature-dependent thermal conductivity. The lower layer has a greater conductivity with little temperature dependence. (b) Results from models in which the entire surface layer has the thermophysical properties of the bottom (Model BOT, dashed) or top (Model TOP, dotted) layer of the two-layer model. (c) Model TWO at 85°N. (d) Models BOT and TOP at 85°N.

lunar Model TWO are very close to those of lunar Model TOP. The penetration depth increases with latitude on the Moon as the seasonal component of the insolation cycle becomes more significant. At the pole, the temperature oscillation penetrates approximately $12^{1/2}$ or 3.5 times deeper into the regolith than at the equator.

Surface and subsurface temperatures as functions of latitude on Mercury and the Moon are shown in Fig. 5. The maximum surface temperature (the radiative equilibrium temperature) and the constant temperature at depth are plotted for the models described above. The results for longitudes 0°W and 90°W on Mercury also represent longitudes 180°W and 270°W, respectively. Because Mercury's orbital eccentricity is large, the maximum temperature at the equator at 0°W is 130 K higher than that at 90°W. The lunar curves represent all longitudes. Model TOP has the highest temperatures at depth on Mercury because of the effect of radiative conduction. Differences between models are less at the poles because of overall lower temperatures and smaller diurnal temperature variations. The temperatures at depth for lunar Models TWO and TOP are similar because of the relative importance of the top layer in Model TWO.

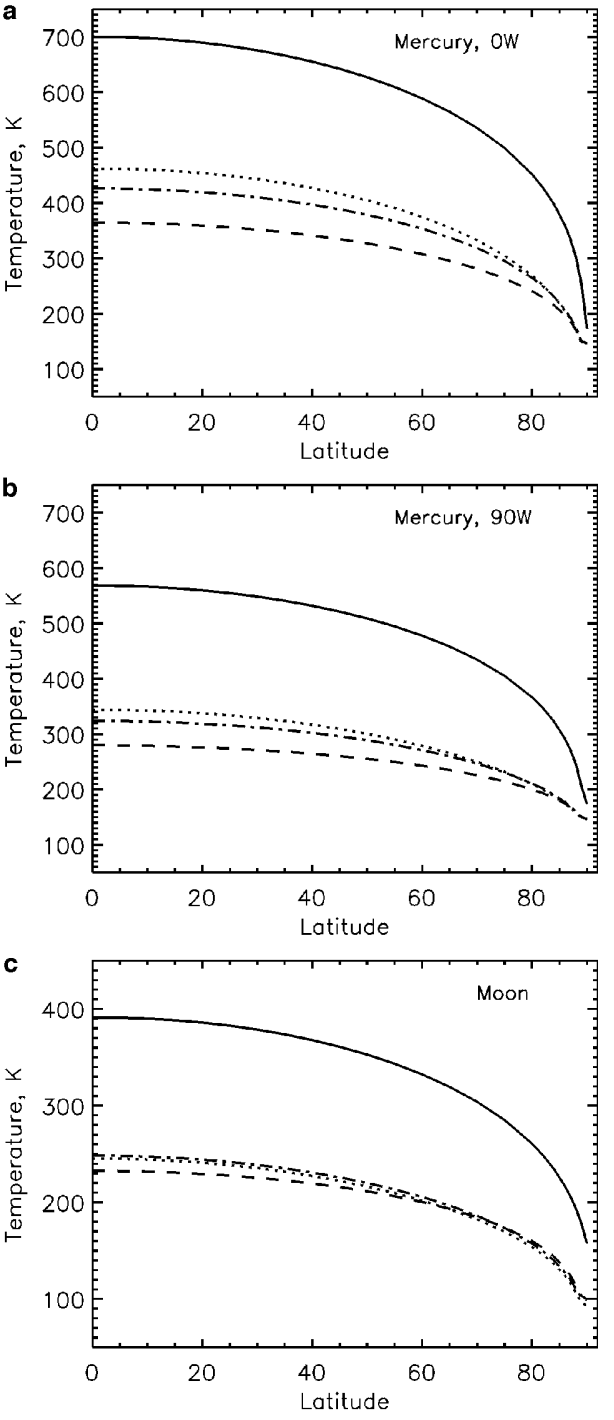

FIG. 5. Maximum surface temperature and temperature at depth as functions of latitude. Sunlit surfaces are in radiative equilibrium and maximum surface temperatures (solid line) are independent of surface thermophysical properties. Planetary heat flow is neglected, so temperature is constant with depth below the attenuation depth of the surface temperature oscillation. Temperatures at depth are shown for the two-layer model (Model TWO, dot-dash) and for models in which the entire surface layer has the thermophysical properties of the bottom (Model BOT, dashed) or top (Model TOP, dotted) layer of the two-layer model. (a) and (b) represent longitudes on Mercury that experience noon at perihelion and aphelion, respectively. (c) Lunar results are independent of longitude.

C. Temperatures within Impact Craters: Motivation

We now extend our model to include the effects of topography, specifically impact craters. Positive topography near the poles of a planet with a small obliquity may prevent poleward areas from receiving any direct sunlight. These permanently shaded areas receive only scattered solar energy and emitted thermal energy from the surrounding topography and energy from the planet's interior. Permanently shaded surfaces are warmed to the extent that they "see" hot, sunlit areas. Temperatures are therefore sensitive to the orientations of the surface and surrounding topography. We consider the permanently shaded areas within the walls of impact craters because of their association with the radar features on Mercury and the ubiquity of craters on the surfaces of both bodies.

The redistribution of energy within a partially sunlit impact crater takes place within a closed system bounded by the crater walls. Scattering models in previous studies were reduced to analytic calculations by assuming that impact craters of all sizes were sections of spheres with varying depth-to-diameter ratios (Paige *et al.* 1992, Ingersoll *et al.* 1992). The flux of scattered radiation is constant for all points within a bowl-shaped crater and the permanently shaded region is isothermal. These calculations showed that water ice is stable to evaporation over billions of years within craters near the poles of Mercury and the Moon, validating the water ice hypothesis. However, detailed comparisons between theory and observation are hampered by the idealized crater morphologies. For example, the latitudinal extent of the features observed on Mercury is significantly greater than that predicted. Only craters with diameters less than 10 km are bowl shaped. Larger craters have broad, flat floors (Pike 1988). These craters may have significantly colder permanently shaded regions (Hodges 1980) and may extend the region of ice stability to lower latitudes.

In order to calculate the temperatures within craters of arbitrary shape, we have created a finite element radiative heat transfer model that accounts for the scattering of solar and infrared energy to all orders and coupled it with our flat surface thermal model. The model steps through time, updating the orbital position and orientation of the planet. The incident solar energy is calculated at each surface element within a bowl-shaped or flat-floored impact crater. We then calculate the multiply scattered components of the solar energy and the emitted infrared energy. The total energy flux incident on each element is fed into the 1-D thermal model, which is run as described in the previous sections. Because of the low albedo of the regolith, infrared radiation from the sunlit portions of the crater dominates scattered solar energy in warming the shaded portions of the craters.

D. Temperatures within Impact Craters: Scattering Model

Each impact crater is modeled as a 32×32 square grid of surface elements. The surface area, height, and orientation at the center of each element are calculated from a spherical section for bowl-shaped craters or a truncated cone for flat-floored craters. The depth, floor diameter, rim height, and rim width as a function of crater diameter have been measured from spacecraft images of Mercury and the Moon and are taken from Pike (1988) and Heiken *et al.* (1991), respectively. Craters up to 10 km in diameter have a depth-to-diameter ratio of about 1 : 5 and are bowl-shaped. Larger craters have relatively more floor area and less steep walls. The depth-to-diameter ratio decreases to ~1 : 25 for 100-km craters. Craters of a given diameter are slightly shallower on Mercury.

At each time step, the model finds the direct insolation incident on each element. Elements can be shaded only by the opposite rim of the crater in the direction of the Sun. The model accounts for the curvature of the planet when calculating the angle to the horizon (the opposite rim) and the angles between elements. The scattering calculations and resulting temperatures are dependent on physical size through the choice of shape parameters and are otherwise independent of scale.

Solar and infrared energy scattered between surface elements is calculated following techniques used in thermal engineering and computer graphics for Lambertian surfaces (Siegel and Howell 1981, Goral *et al.* 1984). The energy transferred from surface element i to j can be mathematically described by defining α_{ij} as the fraction of energy emitted by element i that is incident on element j,

$$\alpha_{ij} = \frac{1}{\pi} \cdot \frac{\cos\theta_i \cos\theta_j \, dS_j}{d_{ij}^2},$$

where θ_i and θ_j are the angles between the surface normals of elements i and j and the line connecting their centers, d_{ij} is the distance between their centers, and dS_j is the surface area of element j. The factor of $1/\pi$ converts between intensity and flux. If F_j is defined as the flux of energy *leaving* element j, then an equation

$$F_j = A_j \cdot \left(\sum_{i=1}^{N} F_i \alpha_{ij} + E_j \right)$$

can be written for all $j = 1, N$ grid elements inside the crater. When calculating scattered insolation, A_j is the albedo of element j and E_j is the direct insolation incident on element j. When calculating scattered infrared energy, A_j is the infrared emissivity and E_j is the blackbody temperature of element j. Simultaneously solving the N equations yields an F_j for each element. The energy absorbed by each element is F_j/A_j. We employ the iterative Gauss–Seidel method to efficiently reduce the matrix. The factors α_{ij} are calculated only once. The direct insolation, multiply scattered insolation, and multiply scattered infrared radiation incident on each surface element at each time step are input to a one-dimensional subsurface thermal model.

We validated our scattering model in several ways. Our results for bowl-shaped craters are identical to the analytic solutions of Ingersoll *et al.* (1992) and Paige *et al.* (1992). Our model is a more complete version of Hodges (1980) and produces similar

results for lunar flat-floored craters. Temperatures of permanently shaded areas from Salvail and Fanale (1994) are higher than ours (e.g., 60 K higher for crater X on Mercury) and those of published analytic solutions. One reason may be that they used an incorrect 59-day diurnal period for Mercury. Our results are independent of the grid size used. Temperatures are sensitive, of course, to the crater shapes used. A discussion of the errors in the crater shape parameters used can be found in Pike (1988). Several effects that we do not account for may reduce temperatures within craters. These include the multiple shadowing effects of small-scale roughness and crater central peaks (Hodges 1980), the higher albedo of the crater floor if covered by ice, and the wavelength- and direction-dependent properties of the surface albedo and emissivity (Mukai *et al.* 1997, Butler 1997).

E. Temperatures within Impact Craters: Results

We modeled hypothetical 10-km bowl-shaped craters, 40-km flat-floored craters, and 100-km flat-floored craters at all locations as well as specific craters observed near the poles of Mercury and the Moon. For Mercury we modeled the craters observed to contain the radar features that are listed in Harmon *et al.* (1994). We estimated their diameters from Davies *et al.* (1978). Tim Colvin of the RAND Corporation (personal communication) provided new estimates of their locations based on a reanalysis of Mariner 10 imagery. A later version of this work was published as Robinson *et al.* (1998). Clementine imagery (Nozette *et al.* 1996) and Arecibo radar maps (Stacy *et al.* 1997) contain the best estimates of the locations of lunar polar craters. Diameters were measured from the Arecibo maps. Locations were taken from the Arecibo maps after shifting the locations of the lunar poles to match Nozette *et al.* (1996). Recent topographic mapping of the lunar polar regions using delay Doppler radar techniques (Margot *et al.* 1997) has produced nearly identical pole positions (Jean-Luc Margot, personal communication). Craters with degraded rims were excluded. The diameters and locations of all modeled craters are listed in Tables I and II and shown graphically in Figs. 6 and 7.

TABLE I
Diameters and Locations of Mercury's Polar Craters

Crater	Diameter (km)	Latitude	Longitude
C	50	87.7 N	171.3 W
D	39	88.3 N	135.4 W
E	28	89.2 N	174.2 W
G	50	86.2 S	73.7 W
L	18	85.3 N	71.9 W
M	35	86.3 N	43.5 W
N	18	85.5 N	10.0 W
P	20	83.5 N	53.9 W
Q	25	82.9 N	45.6 W
R	28	82.8 N	19.4 W
S	21	80.5 N	24.0 W
T	25	80.5 N	20.3 W
U	45	87.1 S	13 W
V	41	81.1 S	84.9 W
W	40	80.7 N	101 W
X	155	88.5 S	147.0 W
Y	15	87.4 N	152.6 W

TABLE II
Diameters and Locations of Lunar Polar Craters

Crater	Diameter (km)	Latitude	Longitude
A (Amundsen)	100	84.7 S	85 E
B	13	89.9 N	90 E
C	19	87.2 N	52 W
F (Nansen F)	60	85.2 N	53 E
G (Gioja)	40	82.8 N	4 W
H (Hermite)	100	85.6 N	85 W
P (Plaskett)	110	82.3 N	179 E
S (Shackleton)	20	89.7 S	111 E
T	32	88.5 S	87 W
U	51	88.1 S	45 E
V	41	87.3 S	82 E
W (Wiechert)	41	84.0 S	163 E
X	33	85.2 S	178 W

Our model output for the 50-km-diameter crater C (87.7°N, 171.3°W) on Mercury is shown in Fig. 8 and illustrates features common to many craters. The figure shows the maximum and average temperatures experienced by each surface element over one diurnal cycle. The permanently shaded region is bounded by a steep gradient of both maximum and average temperature. In this example it covers the equatorward interior wall and entire floor of the crater. The coldest surface elements are located on the crater floor adjacent to the equatorward wall.

III. APPLICATION TO THE STABILITY OF ICE DEPOSITS

In the following sections we discuss the implications of our thermal modeling results for polar ice deposits. We assess the stability of ice deposits by comparing the maximum and average surface temperatures over an insolation cycle with calculated loss rates of volatiles due to thermal sublimation. Because the vapor pressures of volatiles are exponential functions of temperature, sublimation loss rates are controlled by maximum temperatures. Average temperatures are relevant for deposits that are insulated from extreme daytime temperatures, perhaps by burial under centimeters of regolith. Based on the rates shown in Fig. 1, 1 m of water ice evaporates in 1 billion years at a temperature of approximately 110 K. Temperatures of approximately 60, 70, and 220 K are required to sustain deposits of CO_2, NH_3, and S_α (orthorhombic), respectively. The values increase by about 20 K if the time scale is reduced to 1 million years or if the initial thickness is increased to 1 km. We use the above temperature limits to predict where radar-detectable deposits could survive the age of the Solar System. Killen *et al.* (1997) estimate that at temperatures less than ~110 K, the influx of water from meteorites and asteroids balances or exceeds all global losses, providing another reason to suspect that this

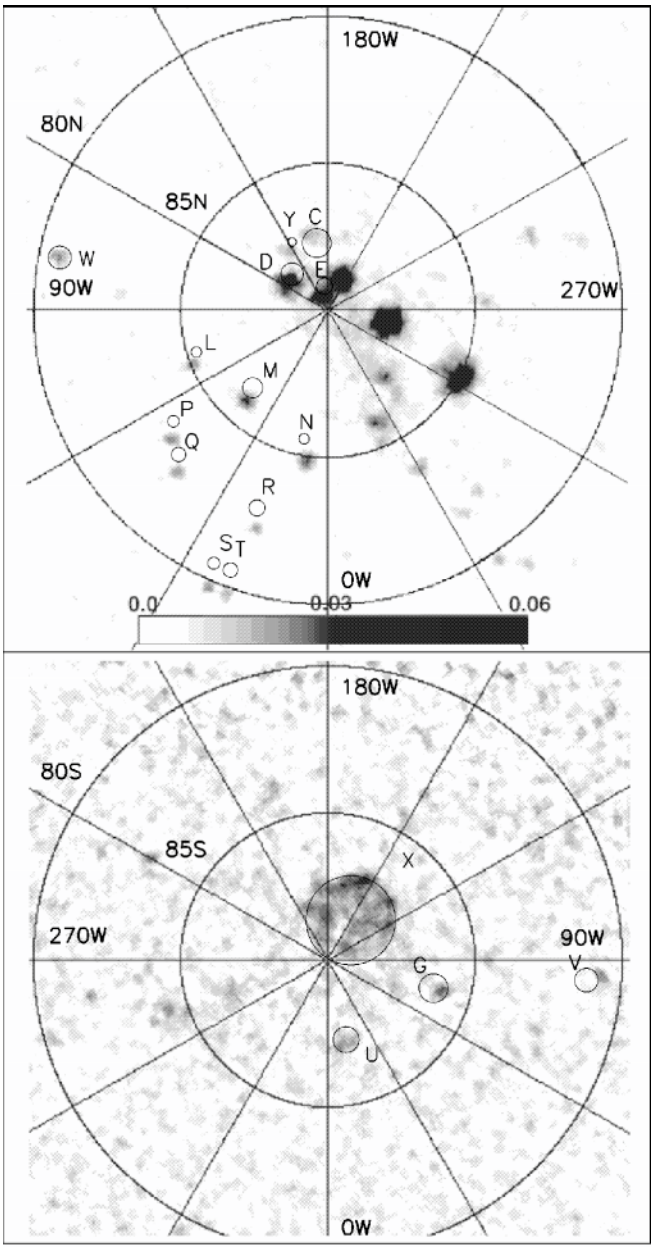

FIG. 6. Locations of impact craters near Mercury's north (top) and south (bottom) poles observed to contain anomalous radar features (Harmon *et al.* 1994). The locations were derived from a recent reanalysis of Mariner 10 data (e.g., Robinson *et al.* 1998). We estimated their diameters from the maps of Davies *et al.* (1978). The crater locations are overlain on Arecibo 13.5-cm radar maps of Mercury's poles, after Harmon *et al.* (1994). The gray levels show specific cross section in the depolarized (unexpected) sense of circular polarization. The spatial resolution is ∼15 km. Harmon *et al.* (1994) estimate that their north pole data should be shifted 1.6° latitude toward 180W longitude (up) and their south pole data should be shifted 1.2° latitude toward 270W longitude (left) to best match the crater locations.

temperature is an appropriate limit for the stability of water ice deposits. We calculate temperatures using bare ground albedos, assuming that all volatiles must migrate to the polar regions and be cold trapped over bare ground.

A. Temperatures of Flat Surfaces

The results for flat surfaces are relevant for continuous deposits (i.e., polar caps or permafrost layers) on or beneath the surfaces of Mercury or the Moon. Figure 5 shows that water ice deposits lying exposed on the surface are not stable on either

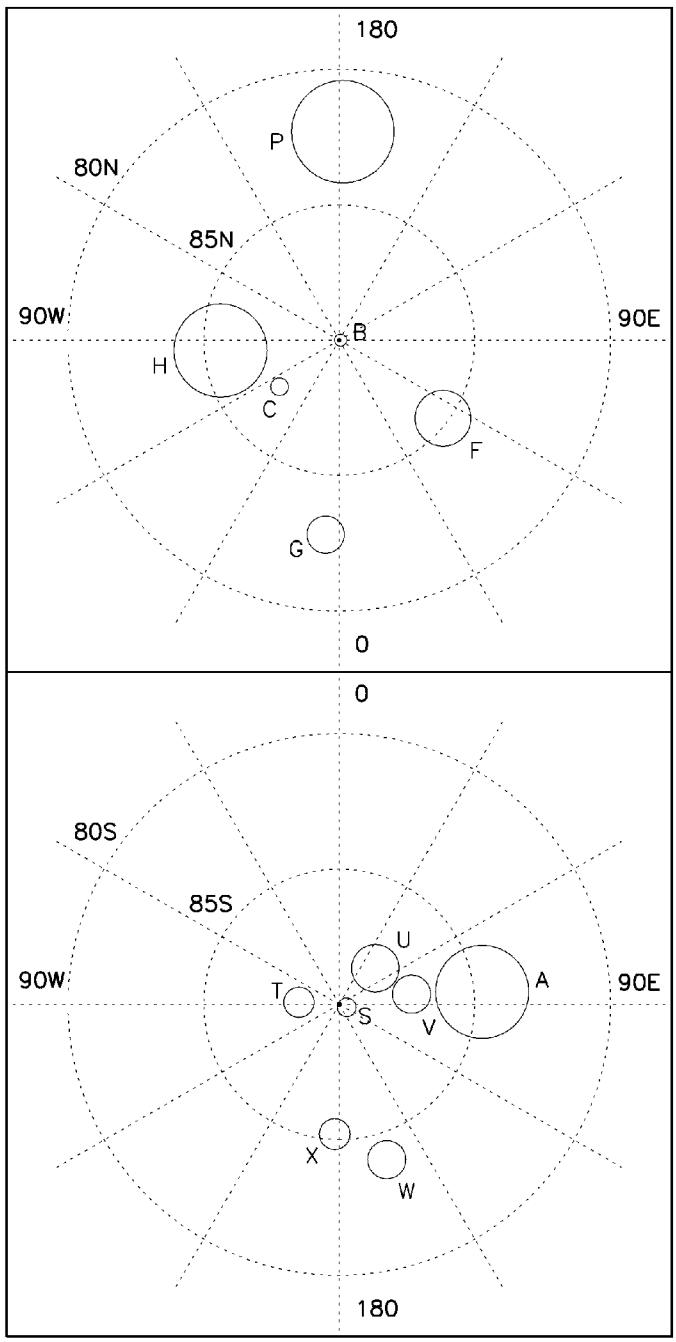

FIG. 7. Locations of impact craters near the Moon's north (top) and south (bottom) poles. Clementine imagery (Nozette *et al.* 1996) and Arecibo radar maps (Stacy *et al.* 1997) contain the best estimates of the locations of lunar polar craters. Diameters were measured from the Arecibo maps. Locations were taken from the Arecibo maps after shifting the locations of the lunar poles to match Nozette *et al.* (1996). Craters with degraded rims were excluded.

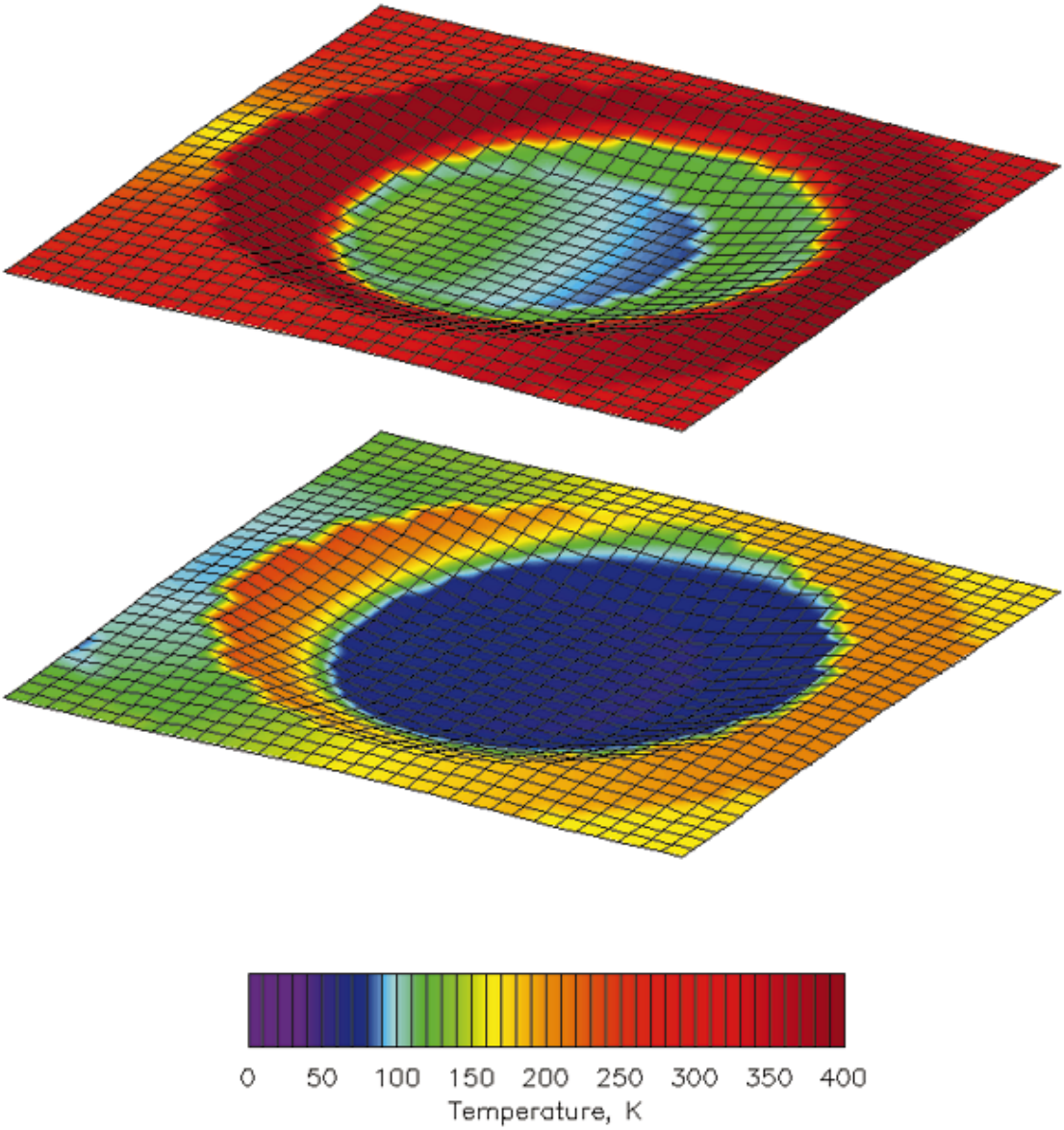

FIG. 8. Diurnal maximum (top) and average (bottom) surface temperatures within crater C (87.7N, 171.3W) on Mercury. The colors represent the maximum and average surface temperature of each element over one diurnal cycle. Permanent shadow covers a large fraction of the crater's interior and is bordered by a large gradient in surface temperature. The coldest region is on the crater floor adjacent to the equatorward rim. At noon the Sun is 2.3° above the horizon toward the lower right. North is toward the upper left.

body. The surface temperature at the pole is 174 K (Mercury) and 159 K (Moon). Buried water ice deposits are stable to thermal sublimation within 2° latitude of the lunar poles. Temperatures at the poles below the extent of the temperature oscillation are 147 K (Mercury) and 93 K (Moon). An exposed polar cap composed of sulfur is stable within 1° (Mercury) and 4° (Moon) latitude of the poles, or 4° (Mercury) and 40° (Moon) latitude if buried.

B. Temperatures within Impact Craters

We use Model TOP for all crater calculations. The choice of Model TOP is justified by its small difference from Model TWO at low temperatures and its relevance for calculating temperatures below a thin regolith cover. More practically, model TWO requires a much smaller time step which makes it prohibitively expensive when used with the scattering model. Temperatures within lunar craters are calculated over one diurnal period at summer solstice and perihelion. The maximum temperatures are the same as if calculated over the full seasonal cycle, but the average temperatures are too large within ∼2° latitude of the pole. A correction can be estimated by comparing the flat surface curves in Fig. 12d with those of Fig. 5. Calculations for hypothetical craters were performed at 0° longitude. The internal heat flux is included because it is important at the low

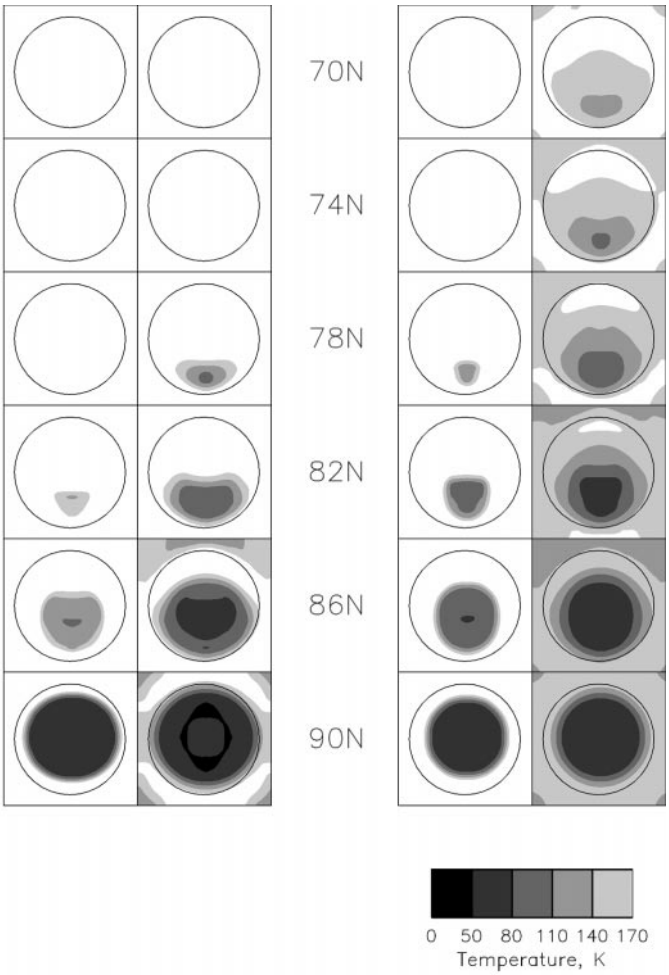

FIG. 9. Diurnal maximum and average surface temperatures within 40-km flat-floored craters on Mercury (left set of columns) and the Moon (right set of columns) at several latitudes. The left column of each set shows maximum temperatures. The right column of each set shows average temperatures. The crater rim is drawn as a solid line. The results also apply to the same latitudes in the southern hemisphere.

temperatures within permanently shaded areas. In these areas, the temperature just below the attenuation depth of the diurnal oscillation is nearly equal to the average surface temperature. Temperature increases with further depth.

Figure 9 shows the maximum and average surface temperatures within 40-km bowl-shaped craters on Mercury and the Moon for latitudes 70°–90°. Figures 10 and 11 show our results for observed craters on both bodies. Figure 12 shows how the thermal stability of ice deposits varies with latitude and crater diameter. The results share some general characteristics. Shallower craters contain colder but smaller permanently shaded areas, and vice versa. In fact, temperatures of permanently shaded regions depend more strongly on crater shape than on latitude. The steeper walls of deep craters receive sunlight at smaller incidence angles and scatter and emit energy more directly toward their interiors. The scattering angle between the sunlit wall and the shaded floor is larger in flat-floored craters than in bowl-shaped craters with the same depth-to-diameter ratio. The angle to the horizon as seen from the crater floor is smaller in shallow craters, which means that they have less permanently shaded area at a given latitude. The physical size of craters matters only for the largest craters, for which the curvature of the planet decreases the visibility of the sunlit walls from the shaded floors, but increases the amount of sunlit area. While the temperature distributions within craters on the Moon are symmetric about the north–south axis (Fig. 11), those of Mercury may be asymmetric depending on the time lag between local noon and perihelion (Fig. 10).

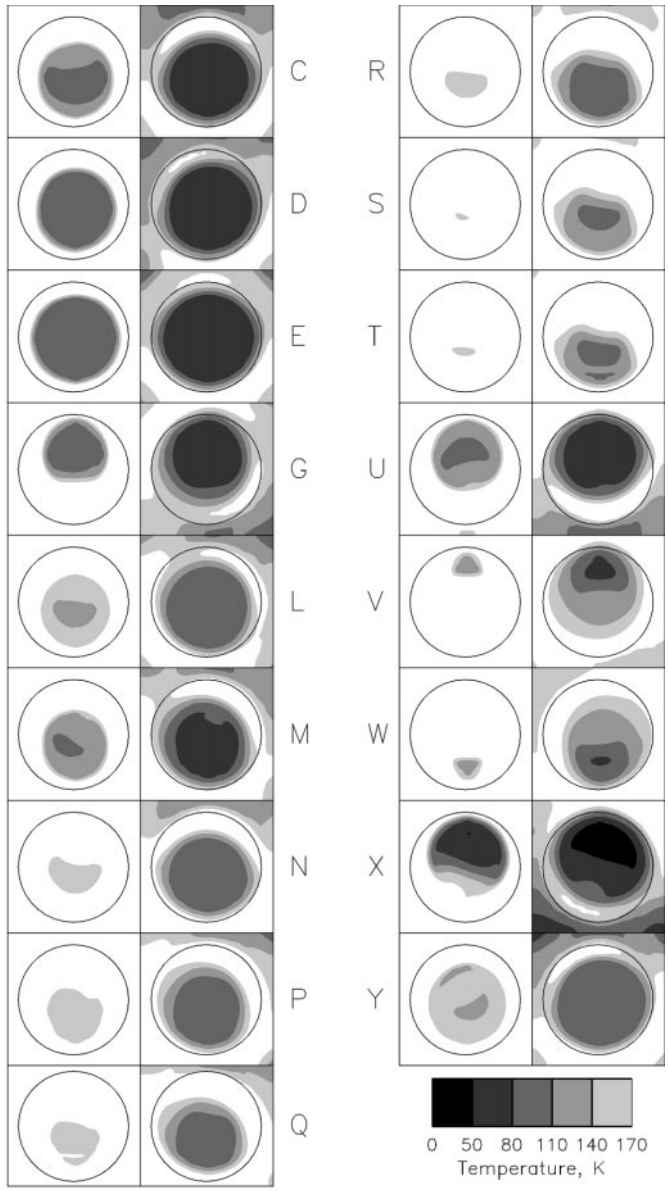

FIG. 10. Diurnal maximum and average surface temperatures within craters observed near Mercury's poles. The left column of each set shows maximum temperatures. The right column of each set shows average temperatures. The crater rim is drawn as a solid line.

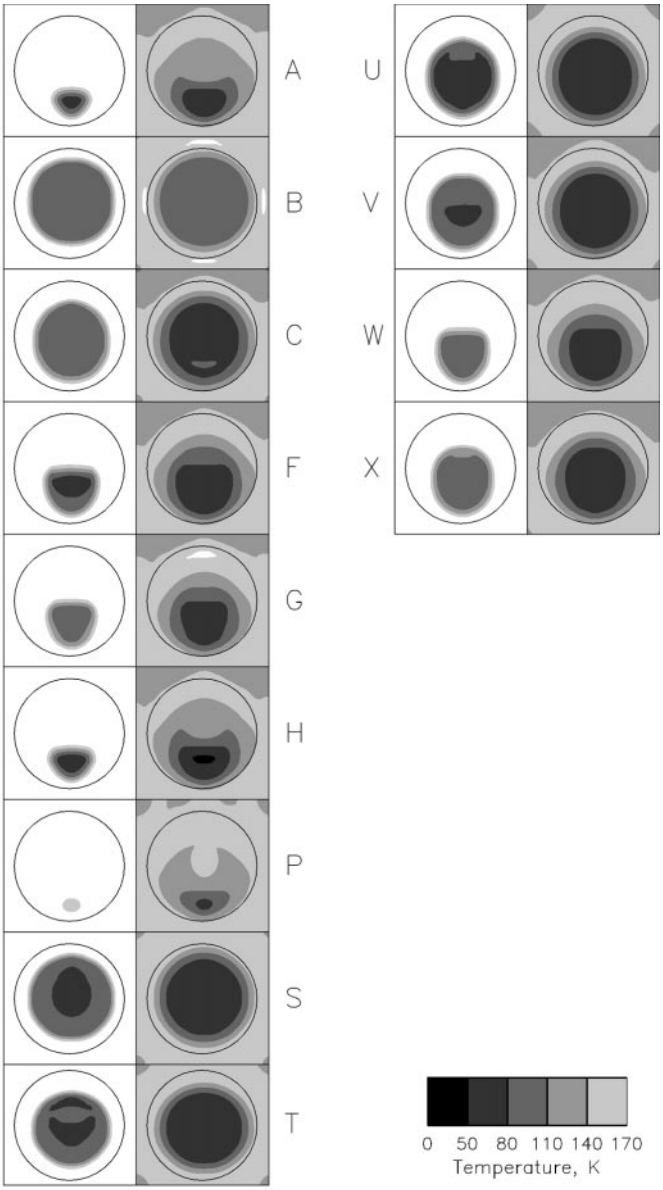

FIG. 11. Diurnal maximum and average surface temperatures within craters observed near the Moon's poles. The left column of each set shows maximum temperatures. The right column of each set shows average temperatures. The crater rim is drawn as a solid line.

Figures 12a–12d show the diurnal maximum and average temperature experienced by the *coldest* surface element within craters on Mercury and the Moon. Flat surface temperatures are shown for comparison. According to Fig. 12a, exposed water ice deposits are not stable within 10-km craters on Mercury. Water ice deposits can survive on the floors of 40-km craters as far as 8° latitude from the poles, beyond which their permanently shaded area is warmer than 110 K. Water ice is stable in 100-km craters as far as 10° latitude from the poles, beyond which they contain no permanently shaded area. Many of the craters on Mercury associated with radar features can have stable water ice deposits exposed on their floors. Figure 12b shows that 10-km craters within 2° latitude of Mercury's poles can harbor water ice deposits if the deposits are protected from extreme surface temperatures. The permanently shaded portions of 40-km craters, 100-km craters, and all observed craters contain regions where average temperatures are below 110 K. Figure 12c shows that exposed water ice deposits would quickly evaporate within 10-km craters on the Moon. Surface deposits can survive within all 40-km and 100-km craters that contain permanently shaded area, and within all observed craters that were modeled. Thermally protected water ice deposits can survive in 10-km craters within about 10° latitude of the poles, as shown in Fig. 12d.

Figure 13 illustrates how the amount of permanently shaded area within craters varies with their diameter and latitude. Very large craters near the Moon's poles have significantly less permanently shaded area than their counterparts on Mercury because of the Moon's greater obliquity. Figure 12 can be used to predict the sizes and the latitudes of craters that contain regions in which ice deposits are stable. The size of the region relative to the size of the crater can then be estimated from Fig. 13.

C. Comparison with Radar Features on Mercury

One of the goals of this study is to better determine the temperatures of surfaces on Mercury that produce ice-like radar responses. How do the results of our model compare with the observed sizes and latitudinal distribution of radar features? The radar maps of Harmon *et al.* (1994), shown in Fig. 6, are a compilation of many observations and have a resolution of ∼15 km. We can make two inferences by comparing our results with specific features. Craters very near the poles of Mercury, such as craters C and D, contain large regions in which surface temperatures never exceed 110 K. The regions where the model predicts stable surface or subsurface ice deposits are consistent with the sizes of the radar features at those locations.

More surprising, radar features are seen within craters where model surface temperatures greatly exceed 110 K, such as craters S and T. The coldest regions within those craters have maximum surface temperatures above 145 K and cover a very small fraction of their crater floors. Most of the floor within each crater is not permanently shaded and experiences much higher temperatures. However, if the stability of these deposits is controlled by the diurnal average surface temperature, our model results are consistent with deposits large enough to produce crater sized radar features.

IV. BURIED ICE DEPOSITS

A. Insulation from Extreme Temperatures

Model calculated surface temperatures within craters N, P, Q, R, S, T, and Y on Mercury are significantly above the limit for long-term stability of water ice. Yet these craters contain large radar features on the Arecibo maps. What accounts for this discrepancy? If the craters were uncharacteristically shallow, their permanently shaded areas would be colder but also smaller. This

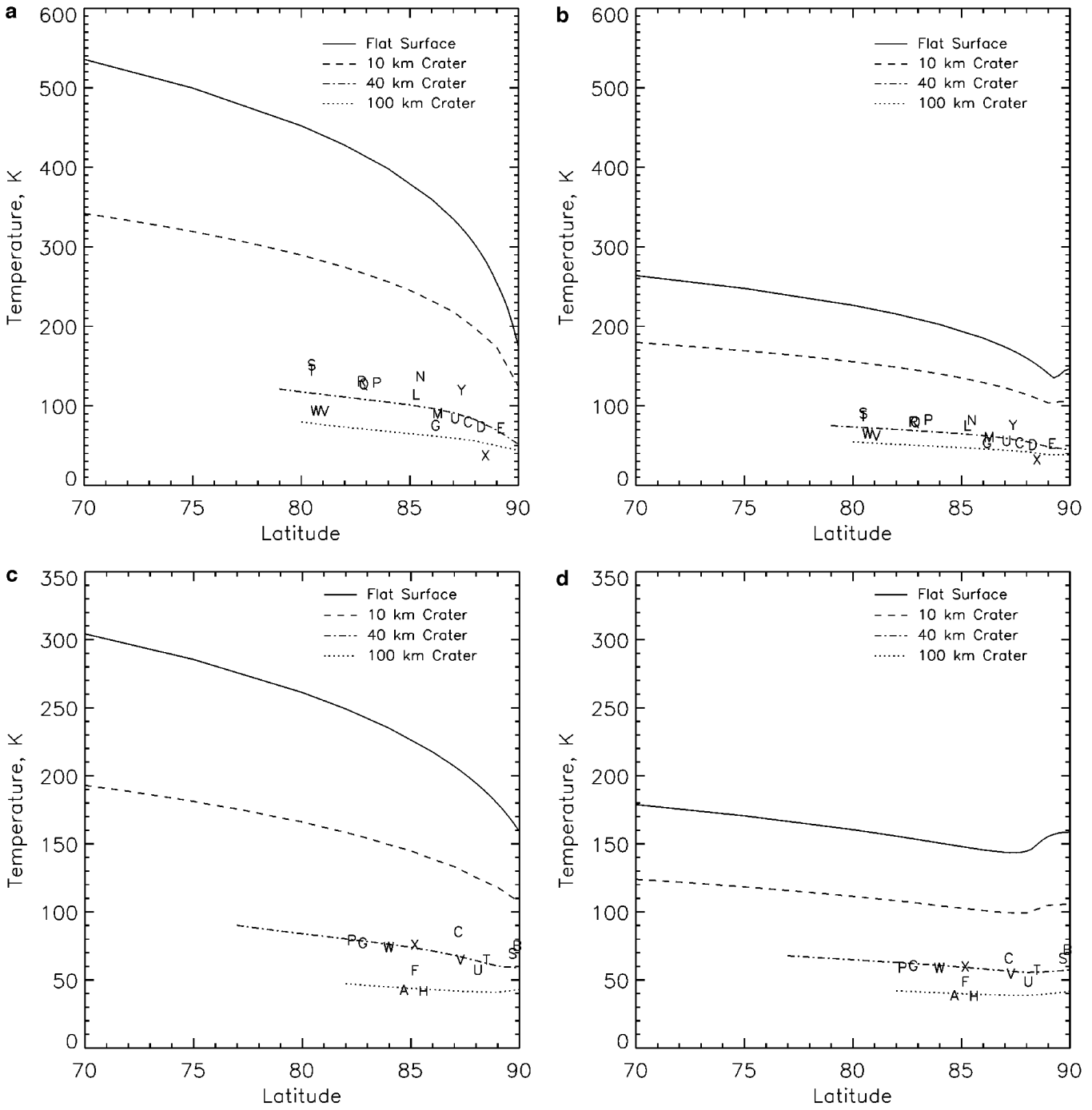

FIG. 12. Diurnal maximum and average surface temperatures within craters on Mercury and the Moon. Curves are shown for 10-km bowl-shaped craters (dashed), 40-km flat-floored craters (dash-dot), 100-km flat-floored craters (dotted), and craters observed near Mercury's or the Moon's poles (lettered). (a) Diurnal maximum surface temperature of the coldest surface element within craters on Mercury. The maximum surface temperature of an unshaded surface is shown for comparison. (b) Diurnal average surface temperature of the coldest surface element within craters on Mercury. In shaded regions the average surface temperature is nearly equal to the temperature just below the attenuation depth of the surface temperature oscillation. The average surface temperature of an unshaded surface is shown for comparison. (c) Same as (a) but for lunar craters. (d) Same as (b) but for lunar craters.

is implausible for craters such as S and T, which already contain small permanently shaded areas. Perhaps our assumed temperature limit should be higher. The limit of 110 K was calculated using vapor pressure data extrapolated by several orders of magnitude beyond lab measurements at 132 K (Bryson *et al.* 1974). However, the limit would have to be ∼150 K for our model to predict surface ice deposits within all of the observed craters. A limit of ∼190 K is more consistent with the sizes of the observed

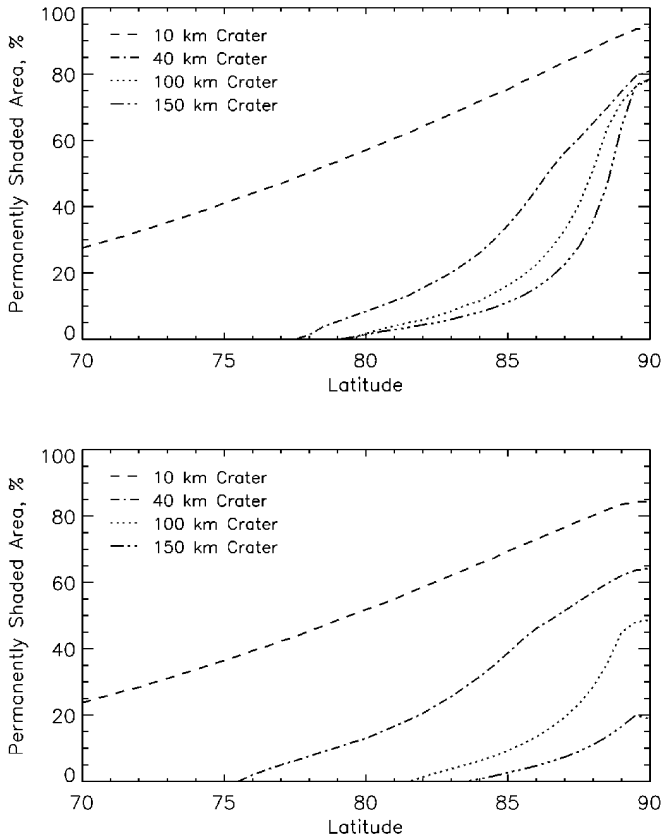

FIG. 13. Permanently shaded area as a function of latitude for impact craters on Mercury (top) and the Moon (bottom). At high latitudes, lunar craters have less permanently shaded area than craters of the same diameters on Mercury because of the Moon's 1.54° obliquity with respect to the Sun.

radar features. At 150 K and 190 K, measured sublimation rates are 1 m per 10^4 years and 1 m per year, respectively, making this explanation implausible. Perhaps the deposits are composed of elemental sulfur and the calculated temperature limit is 220 K. With this limit our model results match the radar features, but as pointed out by Butler (1997), they also predict a (sunlit) surface polar cap 1° latitude wide. A polar cap is neither observed in Mariner 10 imagery nor suggested by the Arecibo radar mapping.

It seems implausible that surface ice deposits are present in several craters that contain radar features. Instead we suggest that the deposits are buried beneath the attenuation depth of sunlight driven temperature oscillations and remain at a constant temperature nearly equal to the average surface temperature. If we compare a limit of 110 K with *average* surface temperatures, our model predicts the sizes and latitudinal distribution of the radar features without also predicting a polar cap on or beneath the surface. A subsurface polar cap would be expected only if the temperature limit were greater than ∼130 K. Our model results are consistent with stable water ice deposits at the locations of all observed radar features if they are thermally protected by burial, although burial is not required for the large craters closest to Mercury's poles. Burial is favorable in other ways not considered in our model. A regolith cover limits evaporative loss by acting as a barrier to diffusing molecules. This could raise the effective temperature limit by tens of degrees Kelvin as discussed in Salvail and Fanale (1994). A thin regolith cover would also protect the deposits from sputtering by solar wind ions and ablation by interstellar UV.

B. Comparison with Observations

We have suggested that lower latitude ice deposits observed on Mercury are thermally protected by a thin regolith layer. Butler *et al.* (1993) suggests that a regolith cover may also explain differences in the radar cross section of the deposits between observations of Mercury at different spatial resolutions and between observations of Mercury and Mars. Butler *et al.* (1993) found relatively low radar reflectivities compared with those of Mars' south polar residual ice cap. The difference could arise if the ice deposits were unresolved or if some energy was absorbed by a regolith cover. If due only to the latter, Butler *et al.* (1993) estimate that a regolith cover with a density of ∼1000 kg m^{-3} would be 0.5 m thick. The higher resolution Arecibo maps revealed that the actual ice coverage within the features described by Bulter *et al.* (1993) may have been as little as 10%. The tradeoff between coverage and absorption, quantified in Fig. 10 of Butler *et al.* (1993), indicates that the regolith layer is probably less than 0.5 m thick. A regolith cover between 0.1 and 0.5 m thick would be sufficient to dampen surface temperature variations without absorbing a significant percentage of the radar signal. Although lunar ice deposits have not been unambiguously detected by radar, the results from the neutron spectrometer aboard Lunar Prospector are consistent (although not uniquely) with the presence of relatively pure water ice buried under tens of centimeters of regolith at the Moon's poles (Feldman *et al.* 1998).

C. Deposition and Burial

Explanations of how ice is deposited and buried are speculative. Water ice is delivered to the surfaces of Mercury and the Moon by comets, asteroids, meteorites, interplanetary dust, solar wind reduction of crustal Fe^0, and outgassing. Several lines of reasoning favor an episodic source, such as one or more comets, because gradually emplaced deposits would be mixed with micrometeoritic material and dust and not be detectable by radar. Morgan and Shemansky (1991) further argue that impact vaporization and interstellar H Lyα could destroy deposits from continuous sources as quickly as they accumulate. More work needs to be done to understand the retention of volatiles after a comet impact, the possible formation of a temporary atmosphere (and a protective ionosphere), and the migration of water to the poles in a collisional atmosphere.

How are the deposits buried, and what controls the depth of burial? Gardening by micrometeorites, which disturbs the regolith and erodes crater walls, is an important and ubiquitous

process on the surfaces of both bodies. Ice deposits might be covered by ejecta or by mass wasting. Killen *et al.* (1997) estimate that local meteoritic impacts and lateral transport of impact debris will form a 1-cm layer in 50 million years. The resulting cover probably would not be uniform. Another possibility is that sublimation results in a self-sealing residue. A slightly dirty ice deposit might sublimate until its contaminant load forms a layer that thermally or diffusively limits sublimation of the underlying ice. The final thickness of the layer would be the attenuation depth of the temperature oscillation if the layer is primarily an insulating layer. Because the diffusion rate is proportional to the regolith temperature, the final thickness of a diffusion limited residue also may be the attenuation depth of temperature oscillations (see Figs. 4 and 10 of Salvail and Fanale 1994). This process requires that a large initial volume of ice be lost to sublimation in order to build the residue.

V. DISCUSSION AND CONCLUSIONS

Nearly every crater on Mercury that has both a relatively undegraded rim and regions where temperatures permit the stability of surface or subsurface water ice also has a radar feature associated with it. In other words, Mercury's available cold traps are full. The Mercury radar features cover roughly 10^{10} m^2, which implies 10^{13} kg of water per meter thickness. Because volatiles will migrate to the coldest cold traps given sufficient time, the presence of ice deposits in warmer, lower latitude craters argues for a large supply of water, a very recent comet impact, or other unexpectedly high supply rates.

Our model results for craters observed near the Moon's poles suggest that lunar cold traps are larger and colder than those within craters on Mercury, mostly because of the smaller solar flux at the Moon. The latitudinal extent of permanently shaded regions is similar on Mercury and the Moon because the increased apparent size of the solar disk at Mercury's orbit and the Moon's small obliquity have similar effects. Several factors other than temperature have undoubtedly influenced whether the Moon's cold traps are as full as Mercury's. The Moon may have had a significantly larger obliquity in its early history (Ward 1975) which would have greatly reduced the amount of cold, permanently shaded area. Whether ancient obliquity variations affect present ice concentrations depends on the history of the sources of volatiles. If impacts of large comets are the primary sources of water ice and occur on billion-year time scales (Arnold 1979), the abundance of ice at a given epoch could vary greatly between the bodies. Impactors will have larger impact velocities at Mercury that may result in less retention of volatiles. A lack of polar topography on the Moon may limit the total volume of deposits, but they could still be detected as long as they are large enough to capture migrating water molecules (Butler 1997) and are resolved by the detection technique. Loss from sputtering by energetic particles may be more significant on the Moon. Without a magnetosphere, the Moon is directly bombarded by the solar wind and repeatedly passes through Earth's geotail where particles directions are more isotropic (Lanzerotti *et al.* 1981).

Several groups propose to use groundbased radar and spacecraft UV spectroscopy, neutron spectrometers, and radar to study potential ice deposits on Mercury and the Moon. Polar orbiting radar systems have the distinct advantage of being able to probe at depth and create maps from an ideal viewing geometry. A combination of radar mapping and supporting image and topographic data will be most useful for comparison with theory and models. Neutron spectrometry does not resolve individual deposits, but is necessary to determine composition. UV spectroscopy and other methods that search for trace exospheric signatures of condensed volatiles may be ambiguous if the deposits are not in diffusive contact with the exosphere. In the long term, *in situ* devices that can withstand the extremely cold temperatures near these deposits will best determine their nature and composition.

Our major conclusions are that (i) water ice deposits on unshaded surfaces (polar caps) are not stable against sublimation over the age of the Solar System on either body, (ii) unshaded subsurface ice is stable within 2° latitude of the lunar poles, (iii) ice deposits within the permanently shaded portions of impact craters are stable as far as 10° and 13° latitude from the poles of Mercury and the Moon, respectively, and (iv) ice deposits are stable within all of the craters observed to produce an ice-like radar response on Mercury, although some deposits must be insulated from extreme daytime temperatures by a regolith cover. Burial under several centimeters of regolith provides protection from several important loss processes and is consistent with observations of ice deposits on both Mercury and the Moon.

ACKNOWLEDGMENTS

We thank John Harmon, Tim Colvin, Jean-Luc Margot, Nick Stacy, Don Campbell, and their respective colleagues for sharing their results. We benefited from the comments of Bruce Murray, Dewey Muhleman, Martin Slade, and two reviewers. A.V. thanks Andy Ingersoll for interest and support of this project.

REFERENCES

Allen, C. W. 1973. *Astrophysical Quantities.* The Althone Press, London.

Arnold, J. R. 1979. Ice in the lunar polar regions. *J. Geophys. Res.* **84**, 5659–5668.

Bryson III, C. E., V. Cazcarra, and L. L. Levenson 1974. Sublimation rates and vapor pressures of H_2O, CO_2, N_2O, and Xe. *J. Chem. Eng. Data* **19**, 107–110.

Butler, B. J. 1997. The migration of volatiles on the surfaces of Mercury and the Moon. *J. Geophys. Res.* **102**, 19283–19291.

Butler, B. J., D. O. Muhleman, and M. A. Slade 1993. Mercury: Full disk radar images and the detection and stability of ice at the north pole. *J. Geophys. Res.* **98**, 15003–15023.

Cremers, C. J., and R. C. Birkebak 1971. Thermal conductivity of fines from Apollo 12. *Proc. Lunar Planet. Sci. Conf. 2nd*, 2311–2315.

Cuzzi, J. N. 1974. The nature of the subsurface of Mercury from microwave observations at several wavelengths. *Astrophys. J.* **189**, 577–586.

Davies, M. E., D. E. Gault, S. E. Dwornik, and R. G. Strom (Eds.) 1978. *Atlas of Mercury.* NASA Scientific and Technical Information Office, Washington, DC.

Feldman, W. C., S. Maurice, A. B. Binder, B. L. Barraclough, R. C. Elphic, and D. J. Lawrence 1998. Fluxes of fast and epithermal neutrons from Lunar Prospector: Evidence for water ice at the lunar poles. *Science* **281**, 1496–1500.

Goldstein, R. M., and G. A. Morris 1975. Ganymede: Observations by radar. *Science* **188**, 1211–1212.

Goral, C. M., K. E. Torrance, D. P. Greenberg, and B. Battaile 1984. Modeling the interaction of light between diffuse surfaces. *Comput. Graphics* **18**, 213–222.

Hagfors, T., I. Dahlstrøm, T. Gold, S.-E. Hamran, and R. Hansen 1997. Refraction scattering in the anomalous reflections from icy surfaces. *Icarus* **130**, 313–322.

Haldemann, A. F. C. 1997. *Interpreting Radar Scattering: Circular-Polarization Perspectives from Three Terrestrial Planets*. Ph.D. dissertation, California Institute of Technology.

Hapke, B. 1990. Coherent backscatter and the radar characteristics of outer planet satellites. *Icarus* **88**, 407–417.

Harmon, J. K., and M. A. Slade 1992. Radar mapping of Mercury: Full-disk images and polar anomalies. *Science* **258**, 640–643.

Harmon, J. K., M. A. Slade, R. A. Velez, A. Crespo, M. J. Dreyer, and J. M. Johnson 1994. Radar mapping of Mercury's polar anomalies. *Nature* **369**, 213–215.

Heiken, G., D. Vaniman, and B. M. French 1991. *Lunar Sourcebook*. Cambridge Univ. Press, New York.

Hodges, R. R. 1980. Lunar cold traps and their influence on argon-40. *Proc. Lunar Planet. Sci. Conf. 11th*, 2463–2477.

Ingersoll, A. P., T. Svitek, and B. C. Murray 1992. Stability of polar frosts in spherical bowl-shaped craters on the Moon, Mercury, and Mars. *Icarus* **100**, 40–47.

Jenniskens, P., and D. F. Blake 1996. Crystallization of amorphous water ice in the Solar System. *Astrophys. J.* **473**, 1104–1113.

Keihm, S. J., and M. G. Langseth, Jr. 1973. Surface brightness temperatures at the Apollo 17 heat flow site: Thermal conductivity of the upper 15 cm of regolith. *Proc. Lunar Planet. Sci. Conf. 4th*, 2503–2513.

Killen, R. M., J. Benkhoff, and T. H. Morgan 1997. Mercury's polar caps and the generation of an OH exosphere. *Icarus* **125**, 195–211.

Langseth, M. G., S. P. Clark, J. Chute, and S. Keihm 1972. The Apollo 15 lunar heat flow measurement. In *Thermal Characteristics of the Moon* (J. W. Lucas, Ed.), pp. 205–232. MIT Press, Cambridge.

Langseth, M. G., S. J. Keihm, and K. Peters 1976. Revised lunar heat-flow values. *Proc. Lunar Planet. Sci. Conf. 7th*, 3143–3171.

Lanzerotti, L. J., W. L. Brown, and R. E. Johnson 1981. Ice in the polar regions of the Moon. *J. Geophys. Res.* **86**, 3949–3950.

Ledlow, M. J., J. O. Burns, G. R. Gisler, J. Zhao, M. Zeilik, and D. N. Baker 1992. Subsurface emissions from Mercury: VLA radio observations at 2 and 6 centimeters. *Astrophys. J.* **348**, 640–655.

Lide, D. R. (Ed.) 1993. *CRC Handbook of Chemistry and Physics*, 74th ed., CRC Press, Boca Raton, FL.

Linsky, J. L. 1966. Models of the lunar surface including temperature-dependent thermal properties. *Icarus* **5**, 606–634.

Margot, J. L., D. B. Campbell, R. F. Jurgens, M. A. Slade, and N. J. Stacy 1997. High resolution topographic maps of the lunar south pole. *Bull. Am. Astron. Soc.* **29**, 986.

Mitchell, D. L., and I. de Pater 1994. Microwave imaging of Mercury's thermal emission at wavelengths from 0.3 to 20.5 cm. *Icarus* **110**, 2–32.

Morgan, T. H., and D. E. Shemansky 1991. Limits to the lunar atmosphere. *J. Geophys. Res.* **96**, 1351–1367.

Morrison, D. 1970. Thermophysics of the planet Mercury. *Space Sci. Rev.* **11**, 271–301.

Moses, J. I., and D. B. Nash 1991. Phase transformations and the spectral reflectance of solid sulfur: Can metastable sulfur allotropes exist on Io? *Icarus* **89**, 277–304.

Muhleman, D. O., B. J. Butler, A. W. Grossman, and M. A. Slade 1991. Radar images of Mars. *Science* **253**, 1508–1513.

Mukai, T., M. Tanaka, H. Ishimoto, and R. Nakamura 1997. Temperature variations across craters in the polar regions of the Moon and Mercury. *Adv. Space Res.* **19**, 1497–1506.

Nozette, S., C. L. Lichtenberg, P. Spudis, R. Bonner, W. Ort, E. Malaret, M. Robinson, and E. M. Shoemaker 1996. The Clementine bistatic radar experiment. *Science* **174**, 1495–1498.

Paige, D. A., S. E. Wood, and A. R. Vasavada 1992. The thermal stability of water ice at the poles of Mercury. *Science* **258**, 643–646.

Pike, R. J. 1988. Impact craters on Mercury. In *Mercury* (F. Vilas, C. R. Chapman, and M. S. Matthews, Eds.), pp. 165–273. Univ. of Arizona Press, Tucson.

Potter, A. E. 1995. Chemical sputtering could produce sodium vapor and ice on Mercury. *Geophys. Res. Lett.* **22**, 3289–3292.

Rawlins, K., J. I. Moses, and K. J. Zahnle 1995. Exogenic sources of water for Mercury's polar ice. *Bull. Am. Astron. Soc.* **27**, 1117.

Rignot, E. 1995. Backscatter model for the unusual radar properties of the Greenland Ice Sheet. *J. Geophys. Res.* **100**, 9389–9400.

Robinson, M. S., M. E. Davies, T. R. Colvin, and K. E. Edwards 1998. Revised positional information for mercurian polar craters. *Proc. Lunar Planet. Sci. Conf. 29th*.

Salvail, J. R., and F. P. Fanale 1994. Near-surface ice on Mercury and the Moon: A topographic thermal model. *Icarus* **111**, 441–455.

Schubert, G., M. N. Ross, D. J. Stevenson, and T. Spohn 1988. Mercury's thermal history and the generation of its magnetic field. In *Mercury* (F. Vilas, C. R. Chapman, and M. S. Matthews, Eds.), pp. 429–460. Univ. of Arizona Press, Tucson.

Siegel, R., and J. R. Howell 1981. *Thermal Radiation Heat Transfer.* Hemispheres, Washington.

Slade, M. A., B. J. Butler, and D. O. Muhleman 1992. Mercury radar imaging: Evidence for polar ice. *Science* **258**, 635–640.

Sprague, A. L., D. M. Hunten, and K. Lodders 1995. Sulfur at Mercury, elemental at the poles and sulfides in the regolith. *Icarus* **118**, 211–215.

Stacy, N. J. S., D. B. Campbell, and P. G. Ford 1997. Arecibo radar mapping of the lunar poles: A search for ice deposits. *Science* **276**, 1527–1530.

Thomas, G. E. 1974. Mercury: Does its atmosphere contain water? *Science* **183**, 1197–1198.

Ward, W. 1975. Past orientation of the lunar spin axis. *Science* **189**, 377–379.

Watson, K., B. C. Murray, and H. Brown 1961. The behavior of volatiles on the lunar surface. *J. Geophys. Res.* **66**, 3033–3045.